encit 2020

ABCM
Associação Brasileira de Engenharia e Ciências Mecânicas

18th Brazilian Congress of Thermal Sciences and Engineering
November 16-20, 2020 (Online)

ENC-2020-0230
NUMERICAL ANALYSIS OF THE AERODYNAMIC PERFORMANCE OF A ROCKET ENGINE COUPLED TO A SCRAMJET DEMONSTRATOR

Felipe Pinheiro Maia
Sandi Itamar Schafer de Souza
Thiago Cardoso de Souza
Federal University of Rio Grande do Norte. Department of Mechanical Engineering. Avenue Senador Salgado Filho, S/N. Mailbox 1524 - Campus Universitário - Lagoa Nova, CEP 59072-970, Natal-RN, Brazil.
felipepm99@hotmail.com, sandi@ufrnet.br, tcardoso@ct.ufrn.br

Abstract. *In this work we analyze the effect of the coupling of a scramjet demonstrator in a brazilian rocket engine in terms of a numerical investigation of the flow around its fuselage geometry. We consider local aspects of the flow and the comparison of global flow parameters, such as the pressure and friction drag, in both geometries. The rocket engine geometry is the brazilian S-30, with the VS-30 rocket as the reference geometry, while the scramjet geometry was selected for operational flight conditions of a Mach number equal to 5.79 and an altitude of 20 km. A set of 2D axisymmetric and planar numerical domains were generated for both geometries. We consider steady-state conditions in all cases, and for the modelling of the turbulent flow, the transition k-kl-ω viscous model was applied. The simulations were able to capture the theoretically expected conical oblique shock and the expansions waves that usually occur for a hypersonic past such geometries. Local effects in the flow were observed such as the emergence of recirculation zones and flow instabilities due to the shock-wave boundary layer interactions. Finally, as a result of the coupling of the scramjet demonstrator to the S-30 rocket engine, the results show an increase in the total drag of about 6.53%.*

Keywords: *Scramjet, VS-30, Shock-Wave Boundary Layer Interactions, Hypersonic Flow, Drag*

1. INTRODUCTION

Currently, one of the most prominent technologies designed for hypersonic flight is the so-called Supersonic Combustion Ramjet (Scramjet), a technology which allows stable combustion under supersonic flow regimes. These engines are designed with a geometry that has ramps and no moving parts and aim to promote oblique shock wave formation as the main flow is admitted in the combustion chamber. These shock waves are responsible for the flow compression and its redirection to the region where supersonic combustion will occur. Figure 1 illustrates a typical example of the geometry of a Scramjet engine.

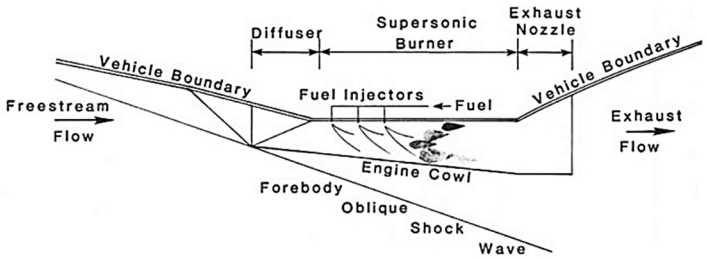

Figure 1. Schematic view of a typical Scramjet engine (Heiser and Pratt, 1994).

The use of an aspirated propulsion engine coupled with a rocket engine is useful as it leads to significantly decreasing of the required oxidant mass in the rocket vehicle, thereby decreasing, for example, related costs with the launch, as pointed out by Rolim et al (2011).

Currently, scramjet technology demonstrators were developed aiming acquisition of flight experimental data (Hass et al., 2005). The design of these demonstrators aims to burn fuel under specific flight conditions, commonly in altitudes ranging from 20 km up to 60 km. In order to perform experiments, these demonstrators are usually coupled to rocket engines to reach its design operational condition, which is established by a specific point along the trajectory of the rocket.

It is expected that the coupling of a scramjet to a rocket engine will significantly affect its flight performance since the external geometry of the vehicle will be modified, and a change in the flow over the vehicle fuselage will naturally

occur. Performance parameters, such as the drag and the lift coefficient, for instance, which are relevant parameters in the development of the rocket trajectory will change due to the replacement of the rocket nose cone by the Scramjet engine.

The objective of this work is to perform a numerical investigation of the flow around the VS-30 rocket engine and over a scramjet geometry coupled to a S-30 rocket engine, in order to analyze and quantify such changes and to investigate if the modified vehicle will reach the desired flight conditions. We intend to quantify the local aspects of the flow that usually develops in the hypersonic regime on both geometries.

In the next section we describe the details of the physical and of the numerical model used in this preliminar investigation.

2. COMPUTATIONAL PROCEDURE

In this paper, a commercial finite volume based CFD solver was used in the investigation of the hypersonic flow (FLUENT 12). The resulting system of governing equations is solved using the compressible formulation for the continuity equation, the Navier-Stokes equations and the energy equation. Turbulence is modelled in terms of a RANS approach with the closure of the turbulent fluxes given by the transition k-kl-ω model. The reason for such choice is due to the fact that this turbulence model is capable of predicting the boundary layer development and the associated transition onset (Moura, 2014). The averaged set of governing equations for the compressible steady turbulent flow is as follows (Versteeg and Malalasekera, 2007):

$$\frac{\partial\left(\overline{\rho}\widetilde{u_i}\right)}{\partial x_i}=0 \tag{1}$$

$$\frac{\partial\left(\overline{\rho}\widetilde{u_j}\widetilde{u_i}\right)}{\partial x_j}=-\frac{\partial\overline{p}}{\partial x_i}+\frac{\partial}{\partial x_j}\left[(\mu+\mu_t)\left(\frac{\partial\widetilde{u_i}}{\partial x_j}+\frac{\partial\widetilde{u_j}}{\partial x_i}\right)\right]+\frac{\partial}{\partial x_j}\left[\frac{1}{3}(\mu+\mu_t)\frac{\partial\widetilde{u_i}}{\partial x_i}\delta_{ij}\right] \tag{2}$$

$$\frac{\partial\left(\widetilde{u_j}\widetilde{T}\right)}{\partial x_j}=\frac{\partial}{\partial x_j}\left[\left(\alpha+\alpha_t\right)\frac{\partial\widetilde{T}}{\partial x_j}\right]+\phi \tag{3}$$

where ρ is the density of the fluid, p the pressure, which is related to ρ in the compressible formulation through the ideal gas state equation: p=ρRT (R is the ideal gas constant). T the temperature, and u_i the velocity field. The variable μ is the fluid viscosity, α the thermal diffusivity of the fluid, μ_t the turbulent viscosity and α_t the turbulent thermal diffusivity, which are closured using the transition k-kl-ω model. In this case an additional set of three transport equations for the turbulent quantities k, kl and ω, not shown here, is coupled to the system of governing equations given by Eqs. 1-3. More details can be found in Walters (2008). The term ϕ is the term of viscous dissipation, defined as follows (Eq. 4):

$$\phi=-\frac{2}{3}\mu\left(\frac{\partial\widetilde{u_i}}{\partial x_i}\right)^2+\frac{\mu}{2}\left(\frac{\partial\widetilde{u_j}}{\partial x_i}+\frac{\partial\widetilde{u_i}}{\partial x_j}\right)\left(\frac{\partial\widetilde{u_j}}{\partial x_i}+\frac{\partial\widetilde{u_i}}{\partial x_j}\right). \tag{4}$$

The index *i* and *j* assume values from 1 to 3. Closely following Versteeg and Malalasekera (2007), the overbar indicates a time-averaged variable and the tilde indicates a Favre-averaged variable. The fluid selected in this work is the calorically perfect air, with viscosity temperature dependence given in terms of the Sutherland viscosity law (Eq. 5).

$$\mu=\frac{C\,T^{3/2}}{T+S} \tag{5}$$

where C and S are empirical constants equals to $1.458\text{x}10^{-6}$ kg/m s $K^{1/2}$ and 110.4 K, respectively (ANSYS, 2009).

The reference geometry of the rocket is the Brazilian VS-30 rocket, a solid propulsion suborbital vehicle whose apogee is within the range of 120-160 km and is propelled by the S-30 rocket engine (Agência Espacial Brasileira, 2019). The geometry of this rocket is designed considering their trajectory curves for flight conditions at Mach numbers of order of M ~ 6. The geometry of the reference rocket is shown in Fig. 2.

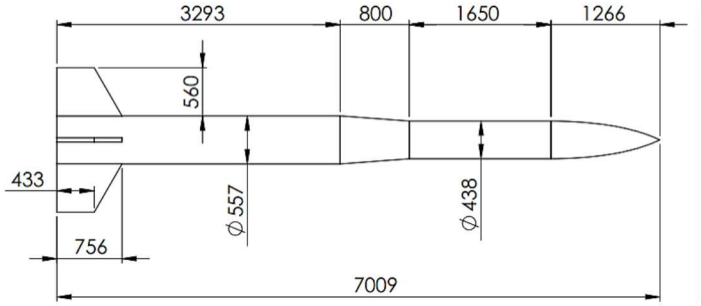

Figure 2. VS-30 rocket engine geometry of the reference case. All units are in mm.

The geometry selected for the scramjet demonstrator, considered in this paper, corresponds to that shown in Pereira (2018), which is designed to operate at a Mach number of 5.79 and an altitude of about 20 km. The designed ramp angles, the calculated shock wave angles and the downstream thermodynamic properties at corresponding flow conditions for the scramjet are summarized in Table 1.

Table 1. Relevant angles and downstream thermodynamics properties. Adapted of Pereira (2018).

Downstream properties	θ (degree)	β (degree)	Pressure (Pa)	Density (kg/m³)	Temperature (K)	Mach number
Free Stream Flow	-	-	5531.00	0.0889	216.65	5.79
Ramp 1	7.25	15.39	14313.39	0.171	291.33	4.86
Ramp 2	8.6	18.42	37035.26	0.329	391.73	4.04
Ramp 3	10.3	22.37	95864.76	0.634	526.81	3.29
Combustion chamber	26.15	43.48	558121.79	1.93	1009.10	1.81

From the defined ramp angles (θ), the entire geometry of the demonstrator is dimensioned (Pereira, 2018). Figure 3 presents in detail the dimensions relevant to this work.

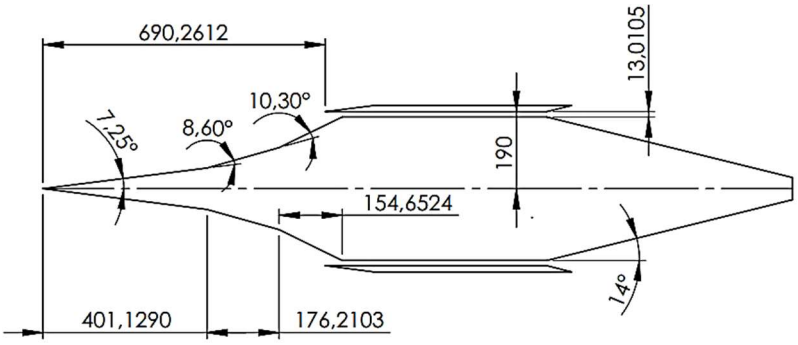

Figure 3. Scramjet geometry for a Mach number of Mach 5.79. All units are in mm.

The scramjet demonstrator was coupled to the S-30 rocket motor using a 800 mm long ramp with an angle of 8.5°. Figure 4 shows the details of the scramjet attached to the rocket engine geometry considered in this work.

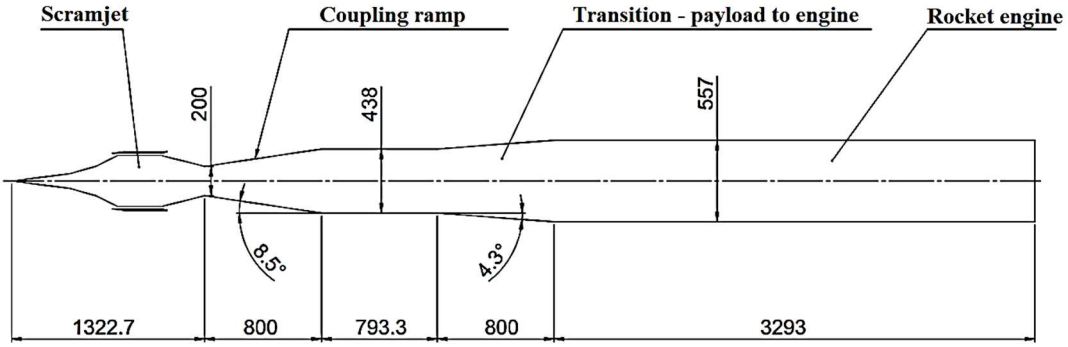

Figure 4. Scramjet coupled with the S-30 rocket engine geometry. All dimensions are in mm.

Next we generate the numerical domain related to the geometries shown in Fig. 2 and Fig. 4. In order to reduce the computational effort, we simplify both geometries assuming, respectively, a 2D planar symmetry for the scramjet and a 2D axial symmetry for the VS-30 rocket and the S-30 rocket engine. Based on such approach, the geometry shown in Fig. 4 was actually divided in two parts: the scramjet with the coupling ramp (planar part) extending from 0 to 2322.7 mm and the S-30 engine with the transition section (axisymmetric part) extending from 2322.7 mm to 7009 mm.

For the spatial discretization of the numerical domains, structured meshes composed of two-dimensional quadrilateral elements in cartesian coordinate were generated. Wall refinement is applied in all cases, with a spatial resolution of 10^{-4} mm in the wall region in order to reach the required condition of $y^+ < 1$. Such choice leads to mesh resolutions of about $4.0x10^5$ elements for the VS-30 rocket, $8.8x10^5$ elements for the scramjet engine with the coupling ramp and $5.4x10^5$ elements for the S-30 engine with the transition section.

Figures 5, 6 and 7 shows the corresponding discretized numerical domains for both cases. The inlet section (i), the outlet section (o), the wall (w) and symmetry (s) regions of the domains are also shown.

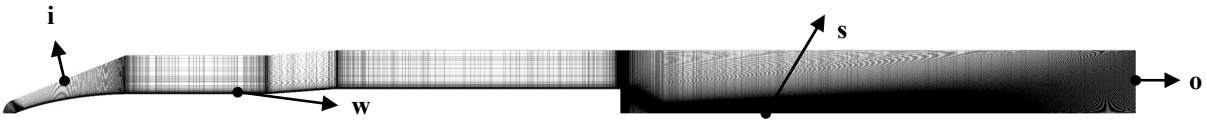

Figure 5. Numerical domain and its corresponding mesh of the VS-30 rocket engine.

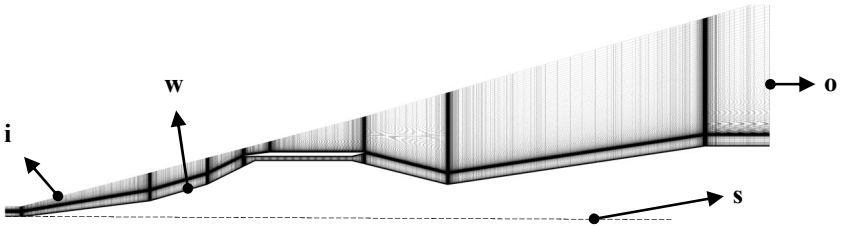

Figure 6. Numerical domain and its corresponding mesh of the scramjet engine with the coupling ramp.

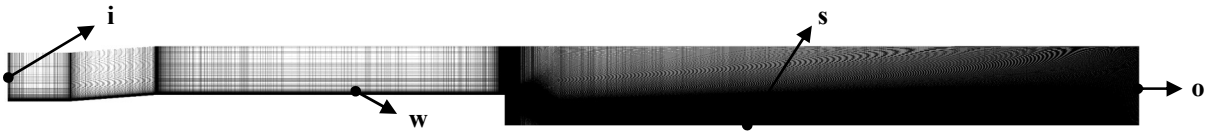

Figure 7. Numerical domain and its corresponding mesh of the S-30 engine with the transition section.

The boundary conditions for both domains are as follows: in the inlet a free stream flow, with properties given in Table 1 (5531 Pa and 216.65 K), is imposed for the pressure and the temperature, while at the walls we set a fixed temperature of 300 K. At the outlet the pressure is set to be equal to the local atmospheric pressure, while for the three velocity components Neumann boundary conditions are imposed, e.g., $\partial u_i/\partial n = 0$, where n is the vector normal to the outlet surface.

For the convective fluxes the first order upwind Roe flux-difference splitting scheme (Roe-FDS) was used (Bigarella and Azevedo, 2012). This scheme guarantees high precision to flows with the presence of shock waves (Blazek, 2015). The option for a first order scheme, in the spatial discretization of the corresponding convective fluxes, was considered in order to ensure numerical convergence, despite the numerical diffusion added to the simulation. Nevertheless, the introduction of such numerical errors are relatively low and does not influence significantly our main results. In fact a separate study, not shown in this paper, was done in order to validate our modelling approach. The solution was considered converged when the residual errors of the equations solved numerically reached values below 10^{-5}, closely following ANSYS (2009). As a secondary criteria, the total drag force and the mass flow rate were additionally monitored.

As Palmerio (2017) pointed out, the total drag force is composed of two components: the pressure drag and the friction drag. Pressure drag is calculated through the integration of the pressure over the surface area of the vehicle (Eq. 6), and the friction drag is calculated by the integration of the wall shear stress over the same surface area (Eq. 7). Only the x-component, which is the component in the flight direction, is considered for the computation of the drag forces.

$$F_{pressure\,drag} = \int_S p\, dS \tag{6}$$

$$F_{friction\ drag} = \int_S \tau\, dS \tag{7}$$

where p is the pressure, τ is the wall shear stress and S the vehicle surface area.

3. RESULTS AND DISCUSSIONS

Figure 8 shows the contours of the Mach number for the VS-30 rocket and for the case with the scramjet coupled to the S-30 rocket engine.

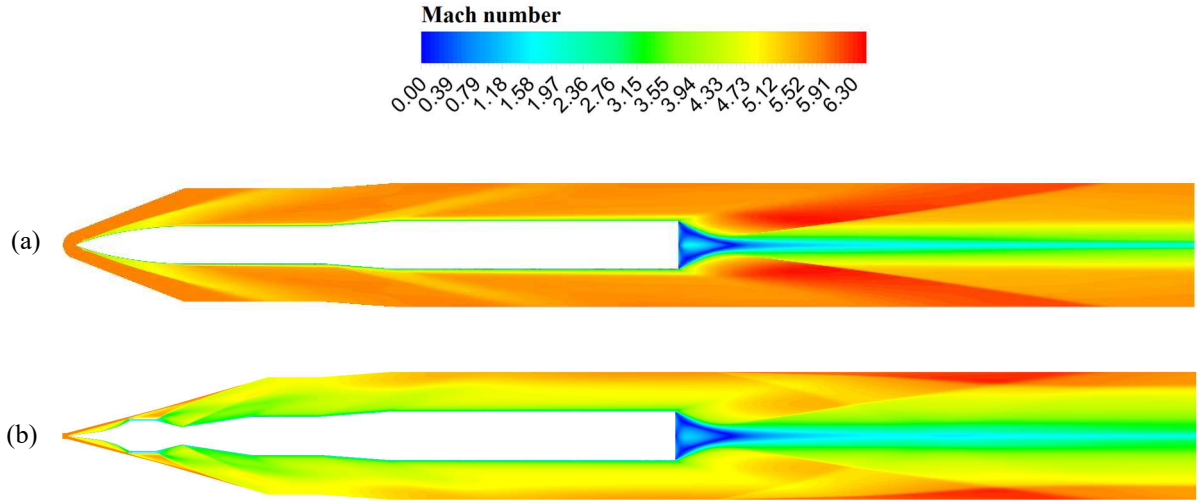

Figure 8. Contours of the Mach number for (a) the VS-30 rocket and (b) the scramjet coupled to the S-30 rocket engine, for an inlet flow with Mach number 5.79 and an altitude of 20 km.

As can be observed, these simulations captured the planar oblique shock waves in the region of the scramjet ramps and also the conical oblique shock waves formed at the nose cone and along the transition ramp of the VS-30 rocket engine. For both cases, the wake region develops at the trailing edge of the rocket engine with an expansion wave arising in this region mainly due to the formation of a recirculation zone. This recirculation flow is the responsible mechanism for the development of a mixing layer at the interface of the trailing wake.

Figure 9 shows the contours of the Mach number for the scramjet model.

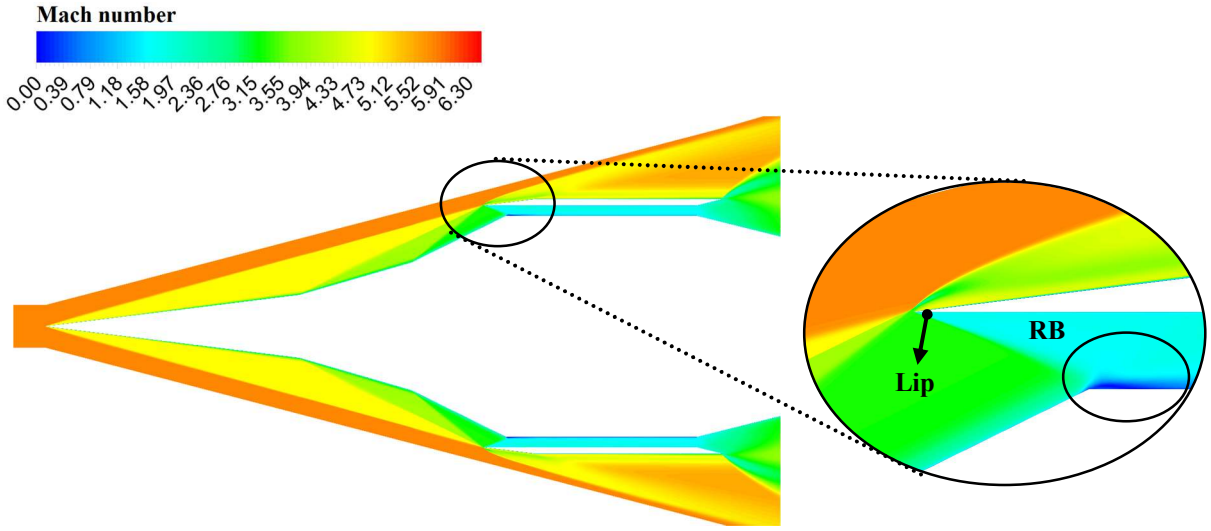

Figure 9. Contours of Mach number for the Scramjet engine. The lip, i.e., the leading edge of the fuselage, are identified, also the recirculation bubble (RB) is highlighted.

In order to maximize the mass of air captured in the combustion chamber, a shock-on-lip condition, i.e., the incidence of the shock wave in the leading edge of the external fuselage, is desired. As Fig. 9 shows, this shock-on-lip condition is not perfectly established, this is largely due to the wall boundary layer which tends to increase the angles of the corresponding shock waves. It can also be seen that a recirculation bubble (RB) develops at the inlet of the combustion chamber, this is a well-known flow instability arising from the interaction between the reflected shock wave and the wall boundary layer (Anderson, 2003). For visualization purposes, Fig. 10 shows the streamlines of the flow in the recirculation

region. A detailed analysis of such flow shows that the Reynolds number in such region is about 10^3, which is typical of such hydrodynamical instabilities (Bejan, 2013).

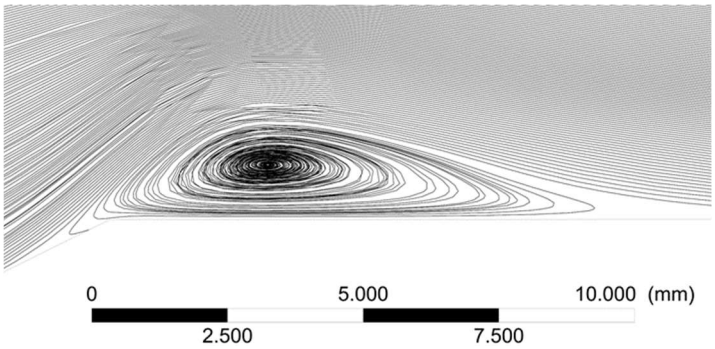

Figure 10. Recirculation bubble in flow streamlines.

Figure 11 presents the contours of the turbulent intensity (defined in terms of Eq. 8) generated for both geometries analyzed in this paper. These contours support the visualization of the points of elevated turbulence in the flow.

$$I = \frac{1}{U}\sqrt{\frac{2}{3}k} \tag{8}$$

where k is the turbulent kinetic energy obtained at point from the corresponding transport equation, U is the inlet velocity, and I is the turbulent intensity.

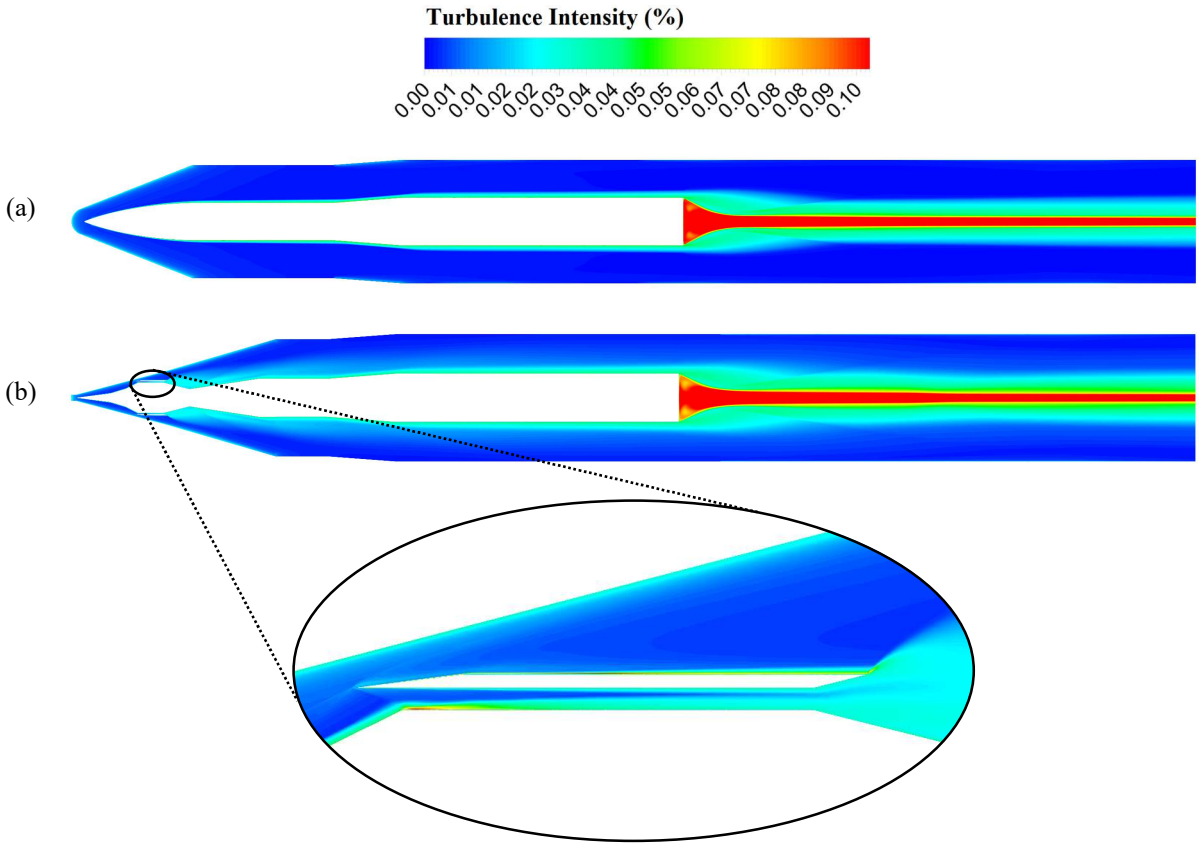

Figure 11. Contours of turbulent intensity. (a) VS-30 rocket. (b) Scramjet coupled to the S-30 rocket engine. The color scale is limited to a maximum value of 10% making it possible to view relevant effects.

Figure 11 (a) shows that in the geometry of the VS-30 rocket, points of elevated turbulence occur in the wake region developed downstream of the trailing edge of the vehicle, this is an expected phenomenon due to the separation of the

flow from the wall and the intense fluid recirculation within such region. For instance, the maximum value of turbulent intensity observed in this geometry is about 21.22%.

As Fig. 11 (b) shows, the recirculation bubble introduces a significant amount of turbulence in the geometry of the Scramjet coupled to the S-30 rocket engine, as can be observed by a peak of turbulent intensity in that region. Such turbulence is carried out by the mean flow further downstream of the geometry, directly interfering with the flow near the wall while promoting a substantial change in the aerodynamic parameters, such as the drag force. High values of turbulent intensity are also found in the wake region formed downstream of the trailing edge of the vehicle, with a maximum turbulent intensity of about 15.85%. For comparison purposes, the turbulent intensity in the recirculation bubble is about of 9.50%.

Figure 12 shows the pressure distribution along the length of both analyzed geometries. As can be observed, the distribution of the pressure is quite different when both cases are directly compared. This is a clearly indication that the pressure drag will be higher when the scramjet geometry is attached to the S-30 rocket engine.

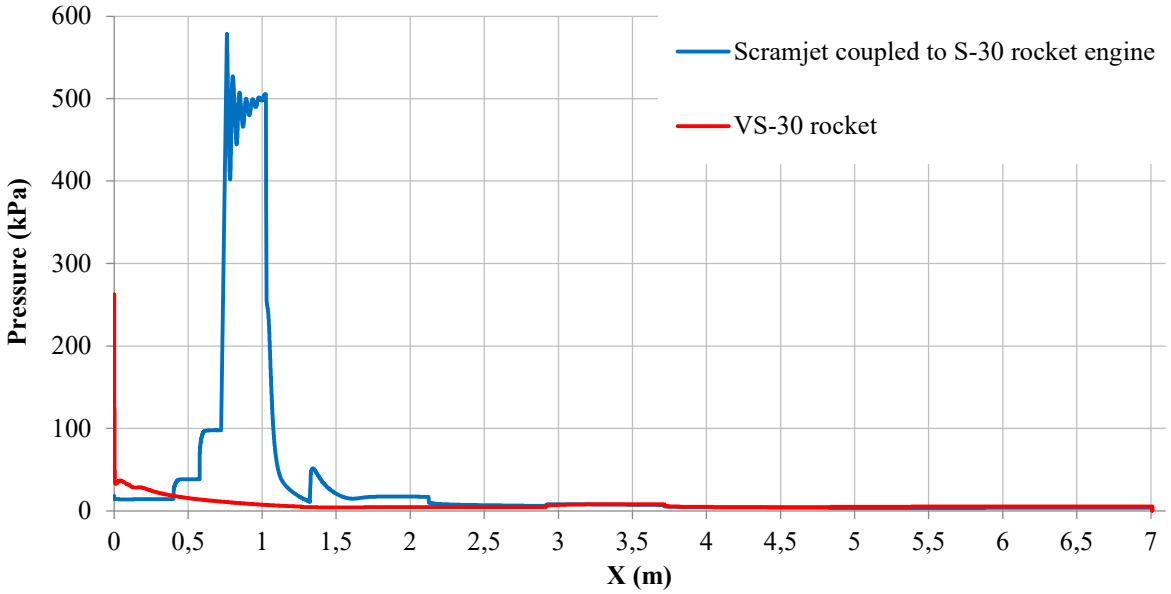

Figure 12. Pressure distribution.

A peak of pressure inside the region of the combustion chamber develops for the rocket engine with the scramjet. Based on these results, Table 2 shows the pressure drag force and the pressure coefficient, Cp, for both cases. The projected area considered in the definition of C_p is 0.2437 m², this area is determined based on the largest diameter of the geometry (557 mm).

Table 2. Pressure drag force and pressure drag coefficient (C_p) of both geometries analyzed in this paper.

	SCRAMJET + S-30			**VS-30**		
	Payload	Rocket body	Total	Payload	Rocket body	Total
Pressure Drag (N)	1434.38	722.52	2156.90	1268.39	744,85	2013,25
C_p	-		0.0681	-		0.0636

As can be seen, the pressure drag value difference between the analyzed cases is 7.14%. For the body of the rocket engine, the pressure drag was essentially the same in both cases. In fact, the main difference is due to the increase in the drag force on the payload region due to the scramjet attachment.

As for the friction drag, Fig. 13 shows the results of the wall shear stress distribution along the length of both geometries. Again, the region of the combustion chamber of the scramjet demonstrator, mostly due to the high temperature of the nearby compressed fluid, generates high levels of wall shear stresses when compared to the VS-30 rocket , i.e., the reference geometry.

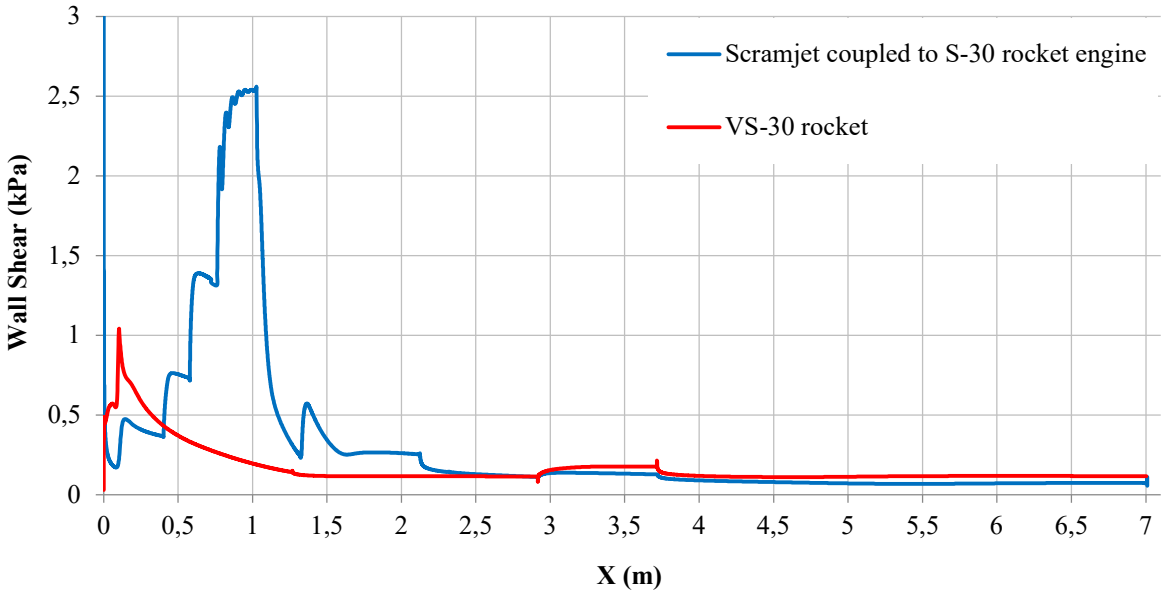

Figure 13. Wall shear stress distribution.

Table 3 shows the friction drag force and the friction coefficient (C_f) for both geometries.

Table 3. Friction drag force and friction drag coefficient (C_f).

	SCRAMJET + S-30			**VS-30**		
	Payload	Rocket body	Total	Payload	Rocket body	Total
Friction drag (N)	652.49	756.36	1408.85	314.01	1019,91	1333,93
C_f	-		0.0445	-		0.0421

The difference in the frictional drag is 5.62%. Table 3 shows that by attaching the scramjet engine to the main rocket engine results in an increase by more than a factor of two of the friction drag force in the payload region. On the other hand, in the rocket engine a decrease of about 300 N in the friction force can be noticed in the scramjet+S-30 case. This result can be explained by the turbulent effects that arise upstream of the flow for such case as shown in Fig. 11, which clearly affect the flow near the wall of the rocket engine.

Finally, we computed the total drag, by adding the friction plus the pressure drag, for both cases. These results are show in Tab. 4.

Table 4 – Total drag force and total drag coefficient (C_D).

	SCRAMJET + S-30	**VS-30**
Total drag (N)	3565.75	3347.18
C_D	0.1126	0.1057

An increase of 6.53% in the total drag for the case scramjet+S-30 is observed when compared with the reference geometry. This clearly indicates that the drag force, which directly impacts in the instantaneous acceleration obtained by the vehicle and the associated velocity developed along the trajectory, might induce a substantial deviation of the previously determined nominal trajectory of the VS-30 rocket engine.

4. CONCLUSIONS

This work is the outcome of an ongoing investigation which intends to quantify the aerodynamics effects resulting of the coupling of a scramjet engine to the S-30 rocket engine. The following conclusions can be established based on the preliminary results presented in this paper:

1. A recirculation zone formed at the trailing edge of the VS-30 rocket engine causes a local expansion wave;
2. The wall boundary layer increases the angle of the oblique shock waves resulting on the non-establishment of the designed shock-on-lip and shock-on-corner conditions;
3. The interaction between the reflected shock wave and the wall boundary layer creates a recirculation bubble, which is an unavoidable flow instability with relevant consequences for the scramjet geometry considered in this investigation;
4. Both geometries presented critical points of turbulence generation. The recirculation bubble induced by the interaction of the reflected shock wave with the wall boundary layer at the entrance of the combustion chamber is largely responsible for the elevated levels of turbulent intensity in the geometry of the case scramjet+S-30;
5. For a flight designed with the specified conditions, e.g., a Mach number of 5.79 and 20 km of altitude, the application of the scramjet demonstrator in the S-30 rocket engine leads to an increase in the total drag of about 6.53%. It is expected that this will induce some deviation in the nominal trajectory of the VS-30 rocket.

5. REFERENCES

Agência Espacial Brasileira, 2019. "VS-30". 30 Oct. 2019 <http://www.aeb.gov.br/programa-espacial-brasileiro/transporte-espacial/vs-30>.

Anderson, J.D., 2003. *Modern Compressible Flow - With Historical Perspective*. McGraw Hill Professional, New York, 3rd edition.

ANSYS, 2009. "ANSYS FLUENT 12.0/12.1 Documentation". ANSYS, Inc. 05 Oct. 2020 <https://www.afs.enea.it/project/neptunius/docs/fluent/>.

Bejan, A., 2013. *Convection Heat Transfer*. John Wiley & Sons, Inc., Hoboken, New Jersey, 4th edition.

Bigarella, E.D.V. and Azevedo, J.L.F, 2012. "A study of convective flux schemes for aerospace flows". *Journal of the Brazilian Society of Mechanical Sciences and Engineering*. Vol. 34, No. 3, pp. 314-329.

Blazek, J., 2015. *Computational Fluid Dynamics: Principles and Applications*. Elsevier Ltd., Baden-Daettwil, Switzerland, 3rd edition

Hass, N.E.; Smart, M. K. and Paull A., 2005. "Flight Data Analysis of HyShot 2". In *13th AIAA/CIRA International Space Planes and Hypersonic Systems and Technologies Conference.* Capua, Italy.

Heiser, W.H. and Pratt, D.T, 1994. *Hypersonic Airbreathing Propulsion*. AIAA Education Series, Washington, DC, 5th edition.

Moura, A.F., 2014. *A computational study of the airfow in Scramjet intakes*. Dissertation of Master in Sciences in Space, Science and Technology, Instituto Tecnológico de Aeronáutica.

Palmerio, A.F., 2017. *Introdução À Tecnologia De Foguetes*. Sindct, São José dos Campos, São Paulo Sindct, 2nd edition.

Pereira, M.V S., 2018. *Projeto aerodinâmico e dimensional de um demonstrador tecnológico scramjet acoplado ao motor foguete S30*. 44 p. Conclusion of an Undergraduate's Project (Undergraduate in Mechanical Engineering) - Universidade Federal do Rio Grande do Norte, Natal-RN.

Rolim, T.C.; Toro, P.G.P; Minucci, M.A.S.; Oliveira, A.C. and Follador, R.C., 2011. "Experimental results of a Mach 10 conical-flow derived waverider to 14-X hypersonic airspace vehicle". *Journal Of Aerospace Technology And Management*, Vol.3, No. 2, pp. 127-136. Institute of Aeronautics and Space. http://dx.doi.org/10.5028/jatm.2011.03027510.

Versteeg, H.K. and Malalasekera, W., 2007. *An Introduction to Computational Fluid Dynamics: The Finite Volume Method*. Pearson Education Limited, Harlow, 2nd edition.

Walters, D.K. and Cokljat, D., 2008. "A Three-Equation Eddy-Viscosity Model for Reynolds-Averaged Navier–Stokes Simulations of Transitional Flow". *ASME Journal Of Fluids Engineering*, Vol. 130, No. 12, 130(12): 121401.

6. RESPONSIBILITY NOTICE

The authors are the only responsible for the printed material included in this paper.